Skyrme forces versus relativistic models: Reexamining instabilities

M. Dutra,[1] O. Lourenço,[1] A. Delfino,[1] J. S. Sá Martins,[1] C. Providência,[2] S. S. Avancini,[3] and D. P. Menezes[3]
[1]*Departamento de Física, Universidade Federal Fluminense, CEP 24210-150 Niterói, RJ, Brazil*
[2]*Centro de Física Teórica, Department of Physics, University of Coimbra, P-3004-516 Coimbra, Portugal*
[3]*Departamento de Física, CFM, Universidade Federal de Santa Catarina, Florianópolis, SC-CP. 476, CEP 88.040-900, Brazil*
(Received 13 September 2007; published 14 March 2008)

Experimental constraints are useful tools in helping to decide, among a number of candidates, which is the more suitable equation of state for nuclear matter. In this work we compare nonrelativistic Skyrme-type and relativistic Walecka-type models when they are used to describe processes related to binary system instabilities and phases coexistence. In general, nonrelativistic and relativistic models predict somewhat different behaviors, but we found that one of the parametrizations of the density-dependent hadronic model shows some similarities with nonrelativistic models in many of the features addressed in our investigation. We have checked that, once experimental data obtained in heavy-ion collisions are extrapolated to account for symmetric and neutron matter, some of the models discussed in the present work, both relativistic and nonrelativistic, should be ruled out.

DOI: 10.1103/PhysRevC.77.035201 PACS number(s): 21.65.−f, 24.10.Jv, 21.30.−x, 21.60.−n

I. INTRODUCTION

Finite nuclei properties and nuclear matter have been reasonably well described by different versions of nonrelativistic and relativistic models.

In principle, there are at least two competing conceptions underlying theoretical approaches to this problem. One can start from a microscopic point of view, by describing the physics of nucleon-nucleon interactions through two-nucleon potentials that fit as well as possible the few-nucleon observables, such as the deuteron binding energy and scattering data [1]. Microscopic models are very important and aim at a full description of nuclear physics. Nevertheless, the many-nucleon properties then derived, usually through (non)relativistic Brueckner-Hartree-Fock (BHF) calculations, present discrepancies even for well-known observables, such as nuclear matter binding energy and its density at saturation, which are in fact correlated [2]. Alternatively, a second approach arises by fitting directly some of the many-nucleon observables based on a mean-field approach, allowing the construction of thermodynamic equations of state to study nuclear matter properties. Next we restrict ourselves to the latter strategy, although it is fair to mention that one of the relativistic models we have chosen to use was parametrized so as to reproduce some microscopic nucleon properties previously obtained through relativistic BHF calculations [3]. The Skyrme force model, one of the most commonly used nonrelativistic models, has been extensively used for a long time. Since one of its first versions [4], the effective Skyrme interaction has been improved and many different parametrizations have been tested. The same has happened with relativistic models, with quantum hadrodynamics (QHD), also known as the Walecka model [5], being one of the most used models. Before embarking on a discussion of nuclear matter instabilities and a comparison between results obtained with both types of models, we revisit some of their history.

In addition to what is already known about Skyrme models [4], we bring here, based on few-nucleon universality properties, a new insight to the understanding of how such a simple model can describe reasonably well nuclear matter properties. It is well known that in few-nucleon physics, the deuteron and triton are low-energy systems with large size scales in which the range of the potential is smaller than the corresponding healing distance of the wave functions. This fact, by itself, allows the nucleons to have a large probability of being outside the interaction range. Therefore, some properties of such systems can be described without detailed knowledge of the nucleon-nucleon interaction but, instead, by assuming a renormalized pairwise s-wave zero-range force [6]. However, in a many-nucleon scenario, dominated by interactions with a range smaller than the nucleon-nucleon scattering lengths, and by considering the triton and ^{4}He nuclear sizes as large as the force range, the picture of a nucleus would be one of a many-body system with the wave function being an eigenfunction of the free Hamiltonian almost everywhere. In addition, the Pauli principle allows only up to four nucleons in the same state, forbidding certain particular configurations in which more particles would overlap. Under such assumptions, it was conjectured that the details of the long-wavelength structure of nuclei may be given by the free Hamiltonian and by few-nucleon scales, which determine the wave function at short distances [7]. This phenomenology is strongly based on the Thomas-Efimov effect [8] and is valid only in the nonrelativistic regime. We believe that such considerations are the reason why contact interaction models, such as those based on Skyrme forces [9], with zero range, describe reasonably well some properties of many-nucleon systems.

Now we move to relativistic models. In its simplest version, the Walecka model for infinite nuclear matter [5], based on relativistic field theory in a mean-field approach, depends, in principle, on four parameters. These are the scalar (vector) $m_\sigma (m_\omega)$ meson masses and the $g_\sigma (g_\omega)$ meson-nucleon coupling constants. However, in the equations of state these constants curiously combine in such a way that only the dependence on $C_\sigma^2 = g_\sigma^2 M^2/m_\sigma^2$ and $C_\omega^2 = g_\omega^2 M^2/m_\omega^2$ appear, where M is the nucleon mass. Therefore, since C_σ^2 and C_ω^2 are fitted to reproduce the nuclear matter bulk properties,

values of m_σ and m_ω become irrelevant in the Walecka model for infinite nuclear matter in a mean-field approach, which cannot distinguish between arbitrary values of mesonic masses. Indeed, in the limit of infinite mesonic masses, the Walecka model provides the same equation of state obtained in its original formulation [10]. However, the Walecka model does not allow for saturation in its nonrelativistic limit and still needs relativistic corrections to avoid the collapse of the system. This can be seen when we consider the nonrelativistic limit of the nuclear matter energy per nucleon, $E_{\rm NR} = (C_\omega^2 - C_\sigma^2)\rho/2M^2 + (3/10M)(3\pi^2\rho/2)^{2/3}$, where ρ is the baryon density. As ρ increases, because the scalar coupling constant is greater than the vector one, the first term dominates, preventing any saturation. It is precisely a relativistic mechanism that is responsible for saturation in most relativistic models.

Although the Walecka model was successful in describing nuclear matter saturation, it unfortunately failed to reproduce its incompressibility. More adequate versions of the Walecka model were developed, and its nonlinear version, the nonlinear Walecka model (NLWM), includes scalar [11] and sometimes vector meson self-interactions [12]. Density-dependent hadronic models (DDHMs) were also constructed as an extension of the NLWM, and the density dependence is normally introduced through the couplings [3,13,14] or through different meson field interactions [15].

The nonrelativistic limit of the NLWM for infinite symmetric nuclear matter has been qualitatively discussed in connection with the Skyrme model [16]. In this case, the cubic nonlinear self-interaction of the scalar field is introduced to rescue nonrelativistic saturation. As already mentioned, with new free parameters given by the nonlinear self-interactions of the scalar field, the Walecka model was then improved to fit observables such as the nuclear matter incompressibility and the spin-orbit splitting of finite nuclei. As a side remark, note that there is a correlation between the effective nucleon mass (m^*) at the saturation nuclear matter density and the spin-orbit splitting for several nuclei [17]. This correlation assures good theoretical L-S splittings for several finite nuclei if m^* lies between 0.58 and 0.62.

In general, relativistic hadronic models have a relativistic mechanism for nuclear matter saturation, which occurs at a density at which the scalar and the vector potentials largely cancel each other. However, nonrelativistic saturation mechanisms may be obtained from Yukawa-type interactions, which are repulsive at very short distances and attractive at a medium range.

In a recent work [18] a low-density expansion of the NLWM energy functional for various parametrizations was performed and the role of the isospin was investigated. It was shown that for the isoscalar channel all the relativistic models considered behave in a similar way. This is true for the binding energy, isoscalar interaction term, and effective mass. The relativistic density-dependent models give a closer description to the one obtained by the nonrelativistic models. The isovector channel has proved to be a different problem: There is a quite big discrepancy even between models within the same framework. Relativistic models generally give a very poor description of this channel.

In the present work we compare, for asymmetric nuclear matter, hadronic relativistic models with some nonrelativistic parametrizations of the Skyrme model. We study thermodynamic instabilities and phase coexistence. We shall see that, even in a nonrelativistic model that follows very closely the behavior of a relativistic model for some bulk properties, the situation may change when we address some specific issues within the instability region of the phase diagram, such as, for instance, the isospin distillation process. In Sec. II we present the formalism for nonrelativistic and relativistic approaches. In Sec. III we display the boundaries of phase coexistence (binodal) for the models and present their critical parameters. In Sec. IV we discuss the instability regions connected to spinodals, neutral charge matter under β equilibrium, isospin distillation, and stellar matter. In Sec. V we investigate the high-density region of the models regarding experimental predictions [19]. Finally, in Sec. VI the main conclusions are summarized.

II. FORMALISM

We start by outlining the main properties and displaying the most important equations of the Skyrme-type and relativistic models we want to discuss in the present work.

A. Skyrme-type models

The Skyrme interactions are normally parametrized through four parameters, t_0, t_1, t_2, and t_3. At the microscopic level, the claim is that t_1 and t_2 account for finite-range effects acting on even- and odd-parity states, whereas t_0 and t_3 are the strengths of zero-range two- and three-nucleon interactions, respectively. In a standard mean-field approach for symmetric nuclear matter at zero temperature, this model furnishes the following energy per nucleon [4]:

$$E(\rho) = T_0(\rho/\rho_0)^{2/3} + \tfrac{3}{8}t_0\rho + \tfrac{1}{16}t_3\rho^{1+\sigma} + \tfrac{3}{80}(3t_1 + 5t_2)\rho k_F^2, \quad (1)$$

where $T_0 = 3k_F^{0^2}/10M$ is the average kinetic energy, $\rho = (2/3\pi^2)k_F^3$ is the nuclear density, M is the nucleon mass, k_F is the Fermi momentum, and σ is a model-dependent parameter. At saturation, ρ and k_F are designated by ρ_0 and k_F^0. Note here that t_1 and t_2 combine together in the mean-field approach to form a single strength parameter.

We start by generalizing for finite temperature and asymmetric nuclear matter Skyrme equation of state (EoS). For $T = 0$ MeV, the corresponding energy density can be found in Ref. [20]. Here, we present the pressure,

$$P = \frac{t_0}{8}\rho^2[2(x_0+2) - (2x_0+1)H_2] + \frac{t_3}{48}(\sigma+1)\rho^{\sigma+2} \times [2(x_3+2) - (2x_3+1)H_2] + \frac{1}{8}\left(\frac{3\pi^2}{2}\right)^{2/3}\rho^{8/3}(aH_{5/3} + bH_{8/3}) + \frac{2}{3}\int d^3p\,\frac{p^2}{2M}\frac{1}{e^{\beta(p^2-p_{Fq}^2)/2M}+1}, \quad (2)$$

TABLE I. Parameters of Skyrme models.

Force	PRC45 [22]	SIII [20]	SLy230a [20]
t_0 (MeV fm^3)	−1089.00	−1128.75	−2490.23
t_1 (MeV fm^5)	0.00	395.00	489.53
t_2 (MeV fm^5)	0.00	−95.00	−566.58
t_3 (MeV fm$^{3+3\sigma}$)	17480.40	14000.00	13803.00
x_0	0.50	0.45	1.1318
x_1	0.00	0.00	−0.8426
x_2	0.00	0.00	−1.00
x_3	−0.50	1.00	1.9219
σ	1	1	$\frac{1}{6}$

with

$$a = t_1(x_1 + 2) + t_2(x_2 + 2), \tag{3}$$

$$b = \tfrac{1}{2}\left[t_2(2x_2 + 1) - t_1(2x_1 + 1)\right], \tag{4}$$

$$H_n(y) = 2^{n-1}[y^n + (1 - y)^n], \tag{5}$$

where the parameters x_1, x_2, and x_3 are given in Table I, $\beta = 1/k_B T$, q refers either to protons (p) or neutrons (n), and the last integral is in fact the sum of two terms, one for each species. The kinetic term in Eq. (2) can be put in the form of a Fermi integral $F_\alpha(\eta_q)$ with $\eta_q(\rho - q, T) = F^{-1}_{1/2}(\sqrt{\pi}\lambda^3\rho_q/2\gamma)$, where $\lambda = \sqrt{2\pi\hbar^2/MT}$ is the thermal de Broglie wavelength, $M = 939$ MeV is the nucleon mass, and $\gamma = 2$ is the degeneracy factor for neutrons and protons separately. The nuclear density is $\rho = \rho_p + \rho_n$ and $y = \rho_p/\rho$ is the asymmetry factor given by the proton fraction.

The Fermi integrals may be expanded in the parameter $\lambda^3\rho$ and they acquire different forms depending on their size [21]. In the regime of a nearly nondegenerate Fermi gas, the resulting EoS has an ideal gas character in leading order plus higher order corrections, and it can be cast in the form

$$\begin{aligned} P = {} & f(T)\frac{\hbar^2}{5M}\left(\frac{3\pi^2}{2}\right)^{2/3}\rho^{5/3}H_{5/3} + \frac{t_0}{8}\rho^2[2(x_0 + 2) \\ & - (2x_0 + 1)H_2] + \frac{t_3}{48}(\sigma + 1)\rho^{\sigma+2}[2(x_3 + 2) \\ & - (2x_3 + 1)H_2] + \frac{1}{8}\left(\frac{3\pi^2}{2}\right)^{2/3}\rho^{8/3}(aH_{5/3} + bH_{8/3}) \\ & + T\rho + \frac{T\lambda^3}{8\sqrt{2}\gamma}[1 + (2y - 1)^2]\rho^2, \end{aligned} \tag{6}$$

where, $f(T)$ is a Kronecker δ symbol δ_{0T}.

In this approximation, the equations of state can be obtained analytically. Indeed, by using the Gibbs-Duhem relation and following the same procedure as developed in Ref. [22], the chemical potentials are given by

$$\begin{aligned} \mu_q = {} & f(T)\frac{\hbar^2}{2M}\left(\frac{3\pi^2}{2}\right)^{2/3}\rho^{2/3}H_{5/3} + \frac{1}{5}\left(\frac{3\pi^2}{2}\right)^{2/3} \\ & \times \rho^{5/3}(aH_{5/3} + bH_{8/3}) + \frac{t_0}{4}\rho[2(x_0 + 2) \\ & - (2x_0 + 1)H_2] + \frac{t_3}{48}(\sigma + 2)\rho^{\sigma+1}[2(x_3 + 2) \\ & - (2x_3 + 1)H_2] \pm \frac{1}{2}[1 \mp (2y - 1)] \\ & \times \left[f(T)\frac{3\hbar^2}{10M}\left(\frac{3\pi^2}{2}\right)^{2/3}\rho^{2/3}H'_{5/3}\right. \\ & - \frac{t_0}{8}\rho(2x_0 + 1)H'_2 - \frac{t_3}{48}\rho^{\sigma+1}(2x_3 + 1)H'_2 \\ & \left. + \frac{3}{40}\left(\frac{3\pi^2}{2}\right)^{2/3}\rho^{5/3}(aH'_{5/3} + bH'_{8/3})\right] \\ & + T\ln\left(\frac{\lambda^3}{\gamma}[1 \pm (2y - 1)]\frac{\rho}{2}\right) \\ & + \frac{T\lambda^3}{2\sqrt{2}\gamma}[1 \pm (2y - 1)]\frac{\rho}{2}, \end{aligned} \tag{7}$$

with the upper sign for protons and the lower sign for neutrons and $H'_n(y) = dH_n/dy$.

For the sake of completeness we also give the energy density divided by ρ:

$$\begin{aligned} \frac{\mathcal{E}}{\rho} = {} & f(T)\frac{3\hbar^2}{10M}\left(\frac{3\pi^2}{2}\right)^{2/3}\rho^{2/3}H_{5/3} \\ & + \frac{t_0}{8}\rho[2(x_0 + 2) - (2x_0 + 1)H_2] \\ & + \frac{t_3}{48}\rho^{\sigma+1}[2(x_3 + 2) - (2x_3 + 1)H_2] \\ & + \frac{3}{40}\left(\frac{3\pi^2}{2}\right)^{2/3}\rho^{5/3}(aH_{5/3} + bH_{8/3}) \\ & + \frac{3T}{2} + \frac{3T\lambda^3}{16\sqrt{2}\gamma}[1 + (2y - 1)^2]\rho. \end{aligned} \tag{8}$$

Let us remark that at finite temperature the expansion used in Eqs. (6)–(8) works well only for $T > 5$ MeV.

The symmetry energy at $T = 0$, $E_{\rm sym} = \frac{1}{8}\frac{\partial^2(\mathcal{E}/\rho)}{\partial y^2}\big|_{\rho, y=0.5}$, is given in these nonrelativistic models by

$$\begin{aligned} E_{\rm sym} = {} & \frac{\hbar^2}{6M}\left(\frac{3\pi^2}{2}\right)^{2/3}\rho^{2/3} - \frac{t_0}{8}(2x_0 + 1)\rho \\ & - \frac{t_3}{48}(2x_3 + 1)\rho^{\sigma+1} + \frac{1}{24}\left(\frac{3\pi^2}{2}\right)^{2/3}\rho^{5/3}[a + 4b]. \end{aligned} \tag{9}$$

The behavior of this quantity as a function of the nuclear density can be seen in Fig. 1. In this figure we have also included, for comparison, the symmetry energies obtained within relativistic nuclear models. The results are discussed in the next section. From the symmetry energy, which is repulsive, the density symmetry, given by the slope of the curve, and the symmetry incompressibility, given by its curvature, are, respectively, defined by

$$\begin{aligned} L = {} & 3\rho_0\left(\frac{\partial E_{\rm sym}}{\partial\rho}\right)_{\rho=\rho_0} = \frac{\hbar^2}{3M}\left(\frac{3\pi^2}{2}\right)^{2/3}\rho_0^{2/3} \\ & - \frac{3t_0}{8}(2x_0 + 1)\rho_0 - \frac{t_3}{16}(2x_3 + 1)(\sigma + 1)\rho_0^{\sigma+1} \\ & + \frac{5}{24}\left(\frac{3\pi^2}{2}\right)^{2/3}(a + 4b)\rho_0^{5/3}, \end{aligned} \tag{10}$$

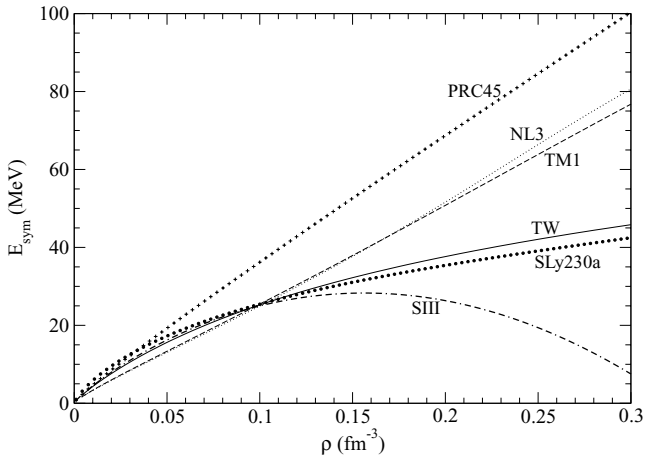

FIG. 1. Symmetry energy versus density.

$$K_{\rm sym} = 9\rho_0^2\left(\frac{\partial^2 E_{\rm sym}}{\partial\rho^2}\right)_{\rho=\rho_0} = -\frac{\hbar^2}{3M}\left(\frac{3\pi^2}{2}\right)^{2/3}\rho_0^{2/3} - \frac{3t_3}{16}(2x_3+1)(\sigma+1)\sigma\rho_0^{\sigma+1} + \frac{5}{12}\left(\frac{3\pi^2}{2}\right)^{2/3}(a+4b)\rho_0^{5/3}, \quad (11)$$

where ρ_0 is the saturation nuclear matter density. These last three quantities allow the construction of an approximate EoS, largely used to study nonrelativistic nuclear matter and finite nuclei behavior [23],

$$\frac{\mathcal{E}(\rho,\delta)}{\rho} = -\frac{B}{A} + \frac{1}{18}(K + K_{\rm sym}\delta^2)\left(\frac{\rho-\rho_0}{\rho_0}\right)^2 + \left[J + \frac{L}{3}\left(\frac{\rho-\rho_0}{\rho_0}\right)\right]\delta^2, \quad (12)$$

where B/A is the nuclear matter binding energy, $\delta = (\rho_n - \rho_p)/\rho = 1-2y$, $J = E_{\rm sym}$, and the volumetric incompressibility at $T=0$ is given by

$$K = 9\left(\frac{\partial P}{\partial\rho}\right)_{\rho=\rho_0} = \frac{3\hbar^2}{M}\left(\frac{3\pi^2}{2}\right)^{2/3}\rho_0^{2/3}H_{5/3} + \frac{9t_0}{4}\rho_0[2(x_0+2) - (2x_0+1)H_2] + \frac{3t_3}{16}(\sigma+1)(\sigma+2)\rho_0^{\sigma+1}[2(x_3+2) - (2x_3+1)H_2] + 3\left(\frac{3\pi^2}{2}\right)^{2/3}\rho_0^{5/3}(aH_{5/3} + bH_{8/3}). \quad (13)$$

The phenomenological EoS, given in Eq. (12), has been used to fit data for a large number of nuclei masses, by using the nonrelativistic Thomas-Fermi statistical model with the Myers-Swiatecki phenomenological nucleon-nucleon interaction [24] and with Skyrme interactions [23]. However, robust experimental data for $K_{\rm sym}$ and L are still missing.

In Table I we show the parameters of the Skyrme models used in the present work.

B. Relativistic models

The Lagrangian density that incorporates two of the most commonly used parametrizations of the NLWM [11,12] reads

$$\mathcal{L} = \bar\psi[\gamma_\mu(i\partial^\mu - g_v V^\mu - g_\rho\boldsymbol{\tau}\cdot\mathbf{b}^\mu) - (M - g_s\phi)]\psi + \frac{1}{2}\left(\partial_\mu\phi\partial^\mu\phi - m_s^2\phi^2\right) - \frac{1}{3!}\kappa\phi^3 - \frac{1}{4!}\lambda\phi^4 - \frac{1}{4}\Omega_{\mu\nu}\Omega^{\mu\nu} + \frac{1}{2}m_v^2V_\mu V^\mu + \frac{1}{4!}\xi g_v^4(V_\mu V^\mu)^2 - \frac{1}{4}\mathbf{B}_{\mu\nu}\cdot\mathbf{B}^{\mu\nu} + \frac{1}{2}m_\rho^2\mathbf{b}_\mu\cdot\mathbf{b}^\mu, \quad (14)$$

where ϕ, V^μ, $\mathbf{b}^\mu$, and A^μ are the scalar-isoscalar, vector-isoscalar, and vector-isovector meson fields, respectively, $\Omega_{\mu\nu} = \partial_\mu V_\nu - \partial_\nu V_\mu$, $\mathbf{B}_{\mu\nu} = \partial_\mu\mathbf{b}_\nu - \partial_\nu\mathbf{b}_\mu - \Gamma_\rho(\mathbf{b}_\mu\times\mathbf{b}_\nu)$, $F_{\mu\nu} = \partial_\mu A_\nu - \partial_\nu A_\mu$, and $\boldsymbol{\tau}$ is the baryon isospin. The parameters of the model are the nucleon mass, of the order of $M = 939$ MeV, depending on the parametrization used; the masses of the mesons m_s, m_v, and m_ρ, which are also model dependent; and the coupling constants between the nucleons and the mesons. Nonlinear σ terms are also included in both parametrizations through the constants κ and λ and a nonlinear ω term is present in the TM1 [12] parametrization through the constant ξ.

The Lagrangian density of the density-dependent model (DDHM) we use next reads

$$\mathcal{L} = \bar\psi[\gamma_\mu(i\partial^\mu - \Gamma_v V^\mu - \Gamma_\rho\boldsymbol{\tau}\cdot\mathbf{b}^\mu) - (M - \Gamma_s\phi)]\psi + \tfrac{1}{2}\left(\partial_\mu\phi\partial^\mu\phi - m_s^2\phi^2\right) - \tfrac{1}{4}\Omega_{\mu\nu}\Omega^{\mu\nu} + \tfrac{1}{2}m_v^2V_\mu V^\mu - \tfrac{1}{4}\mathbf{B}_{\mu\nu}\cdot\mathbf{B}^{\mu\nu} + \tfrac{1}{2}m_\rho^2\mathbf{b}_\mu\cdot\mathbf{b}^\mu. \quad (15)$$

The parameters of the model are again the masses and the couplings, which are now density dependent; that is, Γ_s replaces g_s, Γ_v replaces g_v, and Γ_ρ replaces g_ρ and these density-dependent couplings Γ_s, Γ_v, and Γ_ρ are adjusted to reproduce some of the nuclear matter bulk properties shown in Table II, by using the following parametrization:

$$\Gamma_i(\rho) = \Gamma_i(\rho_0)h_i(x), \quad x = \rho/\rho_0, \quad (16)$$

with

$$h_i(x) = a_i\frac{1 + b_i(x+d_i)^2}{1 + c_i(x+d_i)^2}, \quad i = s, v, \quad (17)$$

and

$$h_\rho(x) = \exp[-a_\rho(x-1)], \quad (18)$$

with the values of the parameters m_i, $\Gamma_i(\rho_0)$, a_i, b_i, c_i, and d_i, $i = s, v, \rho$, given in Ref. [3]. From now on, we refer to this parametrization of the DDHM as TW. This model does not include self-interaction terms for the meson fields (i.e., $\kappa = 0$, $\lambda = 0$, and $\xi = 0$) as in NL3 or TM1 parametrizations for the NLWM.

Within a simple mean-field approximation, the equations for the energy density and pressure in terms of the baryonic density (usually referred to as the equation of state) are easily obtained. If one wants to follow the analytical calculations in detail, refer to Refs. [25,26], among many other papers in the literature.

TABLE II. Nuclear matter properties.

	NL3 [11]	TM1 [12]	TW [3]	SIII [20]	SLy230a [20]	PRC45 [22]
B/A (MeV)	16.3	16.3	16.3	15.9	16.0	15.8
ρ_0 (fm^{-3})	0.148	0.145	0.153	0.145	0.160	0.143
K (MeV)	272	281	240	355	230	362
$E_{\rm sym}$ (MeV)	37.4	36.9	32.0	28.2	32.0	50.3
M^*/M	0.60	0.63	0.56	0.76	0.70	1.00
L (MeV)	123	117	55	10	44	140
$K_{\rm sym}$ (MeV)	108	36	−124	−392	−98	−23

Besides the EoS, the nuclear bulk symmetry energy, the density symmetry, and symmetry incompressibility already discussed in the context of the nonrelativistic models, are also important physical quantities since their values and behavior at $\rho \neq \rho_0$ are still not well established. The values of the symmetry energy are related with studies involving neutron skins, radioactive nuclei, and neutron stars. In general, relativistic and nonrelativistic models give different predictions for the symmetry energy. At $T = 0$ the symmetry energy reads

$$E_{\rm sym} = \frac{k_F^2}{6E_F^*} + \rho\frac{g_\rho^2}{8{m_\rho}^2}, \tag{19}$$

with $k_F = (3\pi^2\rho/2)^{1/3}$ and $E_F^* = (k_F^2 + M^{*2})^{1/2}$. For the model with density-dependent couplings, the g_ρ coupling constant should be replaced by the Γ_ρ coupling.

In Fig. 1 we have plotted the symmetry energy as a function of ρ for densities below $2\rho_0$ and for three different relativistic and nonrelativistic models. The NL3 and TM1 parametrizations have very similar behaviors, whereas TW presents a somewhat different behavior at densities both lower and higher than the nuclear saturation density. In Refs. [25–27] extensive discussions involving the symmetry energy curve, its slope and curvature, and its relation with stellar matter have been presented for the models used in the present work and some others. Among the nonrelativistic models there are large differences in the symmetry energy: (a) PRC45 behaves like NL3 and TM1 with a linear rise with density. This is due to the simple isospin dependence on density of this model for $\sigma = 1$ and $t_1 = t_2 = 0$. (b) SIII has a totally different behavior, becoming negative for a density slightly above $2\rho_0$ and giving rise to an instability. This is a drawback of many Skyrme models [28]. (c) Finally, the parametrization SLy230a, specially designed to describe isospin asymmetric nuclear matter, has a behavior very similar to the relativistic TW model.

In Table II the most important nuclear matter bulk properties are shown for all the models discussed so far. In this table, B/A is the binding energy, ρ_0 is the saturation density, K is the incompressibility, $E_{\rm sym}$ is the symmetry energy, also usually referred to as J, and the effective nucleon mass is M^*. We have also included important quantities for the very low density region (L and $K_{\rm sym}$ as already defined).

The negative values for $K_{\rm sym}$ is characteristic of the nonrelativistic models. It is also remarkable how nonrelativistic SLy230a and relativistic TW models approach one another in the value of the quantities shown in Table II, calculated at the nuclear matter saturation density ρ_o. As we will see, this fact can justify their similar phase diagrams. However, we anticipate that this is not the case for the isospin distillation process.

III. PHASE COEXISTENCE

Once the EoS is obtained, either for a Skyrme-type or a relativistic model, the investigation of phase coexistence by the Gibbs criteria for a two-fluid (or binary) system is possible:

$$P(\rho_a, y_a, T) = P(\rho_b, y_b, T), \tag{20}$$

$$\mu_p(\rho_a, y_a, T) = \mu_p(\rho_b, y_b, T), \tag{21}$$

$$\mu_n(\rho_a, y_a, T) = \mu_n(\rho_b, y_b, T), \tag{22}$$

where a and b refer to different (liquid-gas) system phases. To solve this set of equations, we use the method described in Ref. [29] and summarized next. For a given pressure and temperature, the chemical potentials μ_q are functions only of ρ and y. Then, y_a, y_b, ρ_a, and ρ_b are found by searching for rectangles with horizontal and vertical edges in μ_q versus y diagrams, which amounts to satisfying the Gibbs criteria. The same procedure was used in Refs. [30,31] for different parametrizations of the NLWM. A standard situation is displayed in Fig. 2.

For each value of pressure and temperature we obtain a pair of points (y_a, y_b) that correspond to (ρ_a, ρ_b). By repeating

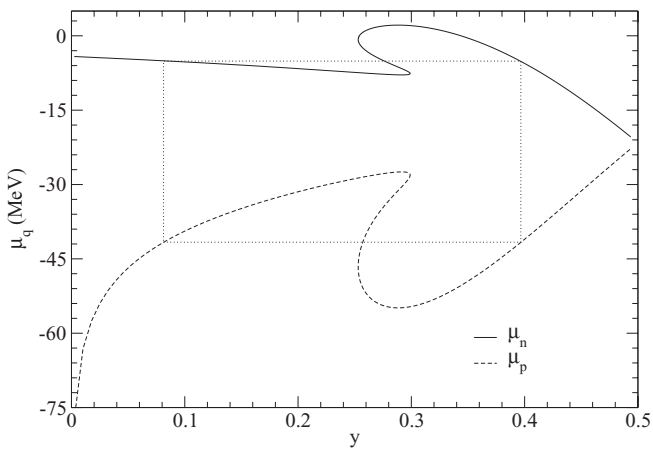

FIG. 2. Geometric construction for the PRC45 model with $T =$ 10 MeV and $P = 0.1$ MeV fm^{-3}.

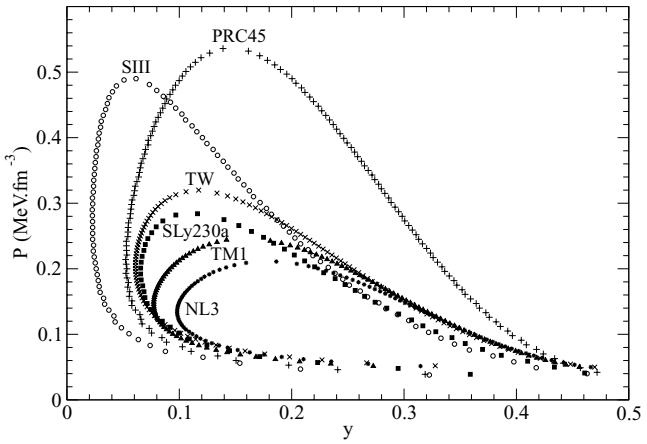

FIG. 3. Binodal section at $T = 10$ MeV.

the same procedure for a range of values of pressure and temperature, the coexistence phase surface (usually called binodal) can be constructed. In Fig. 3 we display a section of the binodal surface at $T = 10$ MeV for the nonrelativistic models (PRC45 [22], SIII, and SLy230a [20]) and the relativistic ones (NL3 [11], TM1 [12], and TW [3]). Differences and similarities are directly related to the way the isovector channel is described in each model, completing the information given by the symmetry energy shown in Fig. 1.

The figure shows that the coexistence points in the phase diagram of the nonrelativistic SLy230a fall close to those of the relativistic model TW, following the same behavior of the symmetry energy displayed in Fig. 1. The parametrizations NL3 and TM1 also show a similar behavior. The Skyrme forces SIII and PRC45 keep apart from all the other models, yielding much larger coexistence regions. These Skyrme parametrizations give a poor description of the isovector channel with several parameters important for the description of this channel equal to zero. For example, for PRC45 the quantities a and b defined in Eqs. (3) and (4) are zero.

Each point (y, P) at the boundary of the binodal section at this temperature represents a stable phase with a definite value of the asymmetry factor y. Points with the same value of P and different values of y represent two stable phases with different proton fractions in mechanical and chemical equilibrium coexisting at the temperature at which the section of the binodal surface was cut. Nevertheless, these points do not represent end points of a phase transition, as opposed to what happens in the usual Maxwell construction for a simple fluid. In binary systems, the constraint of a fixed overall asymmetry factor prevents the phase transition from proceeding isobarically. In other words, if one wants to have end points of the phase transition at the same pressure, the temperature at each of these points has to be different. These considerations justify a somewhat loose terminology that characterizes the line of the phase diagram that connects the end points of an isothermal phase transition as a modified Maxwell construction for binary systems. In this context, for a given temperature, the point of the binodal section that corresponds to the maximum pressure is called a critical point. A line of critical points appear in the phase diagram, one for each temperature, ending at the highest temperature for which a binodal section is still present, at which the critical point corresponds to symmetric matter $y = 1/2$ as seen, for instance, in Refs. [32,33].

TABLE III. Critical parameters.

	T_c (MeV)	ρ_c (fm^{-3})	y_1	y_2
SIII	0	0.1189	0.0041	0.9959
SLy230a	0	0.0843	0.0149	0.9851
PRC45	0	0.0829	0.0402	0.9598
NL3	0	0.0766	0.0567	0.9433
TM1	0	0.0774	0.0496	0.9504
TW	0	0.0818	0.0238	0.9762
SIII	10	0.0810	0.0575	0.9425
SLy230a	10	0.0608	0.1100	0.8900
PRC45	10	0.0692	0.1460	0.8540
NL3	10	0.0573	0.1785	0.8215
TM1	10	0.0601	0.1594	0.8406
TW	10	0.0628	0.1163	0.8837
SIII	20.47	0.0563	0.50	0.50
SLy230a	16.52	0.0535	0.50	0.50
PRC45	20.59	0.0561	0.50	0.50
NL3	14.55	0.0463	0.50	0.50
TM1	15.62	0.0486	0.50	0.50
TW	15.18	0.0509	0.50	0.50

We have also calculated some critical parameters of the nonrelativistic and relativistic models at $T = 0$, $T = 10$ MeV, and $T = T_{c_{\max}}$. In Table III we show ρ_c and the proton fractions for these temperatures.

From Table III, we see that the critical parameters for SLy230a and TW differ very little. The SIII model has the largest isospin asymmetry and largest critical density. The other models have similar critical densities at zero temperature but somewhat different isospin asymmetries, showing that they describe the isospin channel differently. At $T = 10$ MeV, the differences are small, with SIII giving the largest difference. Finally, the critical temperatures are larger for the nonrelativistic models. However, the critical temperature for SLy230a is very similar to the values obtained with the relativistic models. Notice also that the critical temperatures for symmetric matter are generally much lower for relativistic than for nonrelativistic models, except for SLy230a.

IV. INSTABILITIES

In this section we discuss the regions of instability in binary systems. Compared to one-component systems, such as symmetric nuclear matter, there is a reasonable complexity in such a study that deserves a theoretical explanation. After this study, but still in this section, we present some applications.

A. Theory

Inside the coexistence region, there are spinodal regions coming from the mechanical and the chemical instability

regions, which can be found, respectively, by

$$\left(\frac{\partial P}{\partial \rho}\right)_{y,T} = 0 \quad \text{and} \quad \left(\frac{\partial \mu_q}{\partial y}\right)_{P,T} = 0. \tag{23}$$

However, as has been pointed out in Ref. [32], for asymmetric nuclear matter, only the product of these two derivatives define the system instability region.

Notice that at the critical point, which depends on ρ, y, and T, both regions of metastability meet. Note also that the chemical potentials do not depend on the pressure explicitly. Therefore,

$$\left(\frac{\partial \mu_q}{\partial y}\right)_{P,T} = \left(\frac{\partial \mu_q}{\partial y}\right)_{\rho,T} + \left(\frac{\partial \mu_q}{\partial \rho}\right)_{y,T}\left(\frac{\partial \rho}{\partial y}\right)_{P,T} \tag{24}$$

has to be considered. Since

$$\left(\frac{\partial \rho}{\partial y}\right)_{P,T} = -\frac{\left(\frac{\partial P}{\partial y}\right)_{\rho,T}}{\left(\frac{\partial P}{\partial \rho}\right)_{y,T}}, \tag{25}$$

the instability boundaries can be obtained through

$$\left(\frac{\partial \mu_q}{\partial y}\right)_{\rho,T}\left(\frac{\partial P}{\partial \rho}\right)_{y,T} - \left(\frac{\partial \mu_q}{\partial \rho}\right)_{y,T}\left(\frac{\partial P}{\partial y}\right)_{\rho,T} = 0. \tag{26}$$

At this point, we briefly discuss some formal issues concerning the instability criteria. The thermodynamical stability of a system at constant temperature is associated with the convexity of the Helmholtz free energy F. For uniform nuclear matter, F can be given as a function of the state variables ρ_p, ρ_n, and T. So, the convexity of F is equivalent to demanding the positivity of the matrix $\mathcal{F}$, whose elements are defined by

$$\mathcal{F}_{ij} \equiv \left.\frac{\partial^2 f}{\partial \rho_i \partial \rho_j}\right|_T = \left.\frac{\partial \mu_i}{\partial \rho_j}\right|_{T,\rho_i}, \tag{27}$$

where i, j stand for neutron and proton indices. The positivity of $\mathcal{F}$ requires that both of its eigenvalues be positive. Since, for dilute nuclear matter, it happens that one of its eigenvalues is always positive [32], the instability region is determined when the lowest eigenvalue becomes negative. In other words, the boundaries of the spinodal instability region is determined by the condition that det $\mathcal{F}$ vanishes:

$$\left(\frac{\partial \mu_p}{\partial \rho_p}\right)_{\rho,T}\left(\frac{\partial \mu_n}{\partial \rho_n}\right)_{\rho,T} - \left(\frac{\partial \mu_p}{\partial \rho_n}\right)_{\rho,T}\left(\frac{\partial \mu_n}{\partial \rho_p}\right)_{\rho,T} = 0. \tag{28}$$

In fact, the last expression indicates that a unique instability region should be considered instead of a chemical and a mechanical one. As we show in the Appendix, this relation is fully equivalent to the previous one, given by Eq. (26).

It is easy to show that the eigenvalues of $\mathcal{F}$ are given by

$$\lambda_\pm = \frac{\mathrm{tr}\mathcal{F} \pm \sqrt{(\mathrm{tr}\mathcal{F})^2 - 4\det\mathcal{F}}}{2}, \tag{29}$$

where tr$\mathcal{F}$ and det$\mathcal{F}$ are, respectively, the trace and the determinant of $\mathcal{F}$. The corresponding eigenvectors components

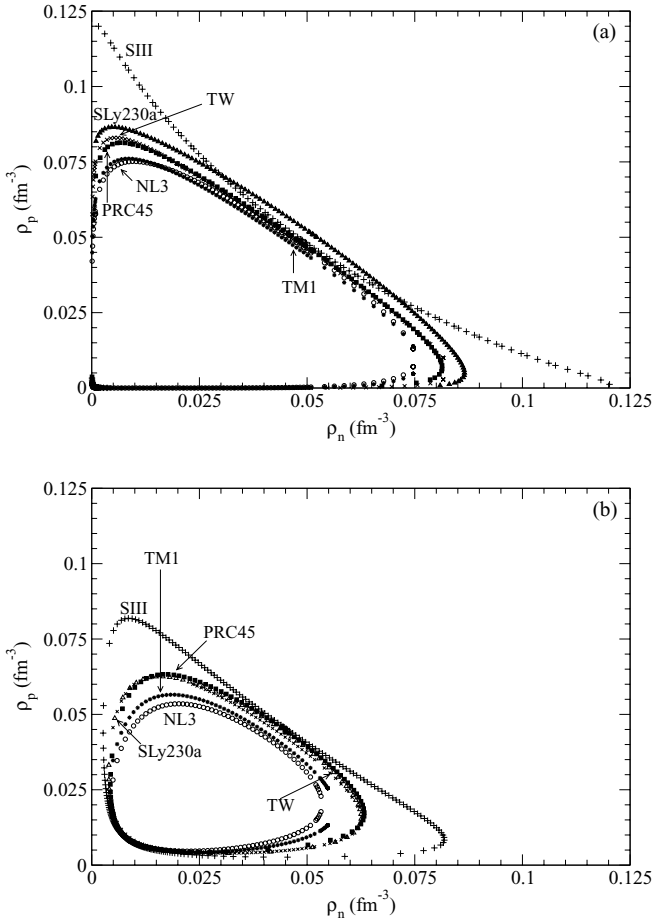

FIG. 4. Spinodal section at (a) $T = 0$ and (b) $T = 10$ MeV.

$(\delta\rho_p^{(\pm)}, \delta\rho_n^{(\pm)})$ satisfy the following relation:

$$\frac{\delta\rho_p^{\pm}}{\delta\rho_n^{\pm}} = \frac{\lambda_\pm - \mathcal{F}_{nn}}{\mathcal{F}_{np}}. \tag{30}$$

Therefore, in a typical situation, the eigenvector associated with a negative λ_- gives the direction of the instability or the direction along which the phase separation occurs. Furthermore, the ratio between its components characterizes the isospin distillation effect, which is discussed later.

B. Spinodals

Any one of the set of Eqs. (26) or (28) has to be solved numerically to obtain the thermodynamical spinodal for a given equation of state. In Fig. 4, for $T = 0$ and $T = 10$ MeV, we show the spinodals for the models we are considering in this work. At both temperatures the SIII spinodal stands out, both because it extends to a larger region for asymmetric matter and because at $\rho_p = \rho_n$ it shows a different curvature. As before, TM1 and NL3 show very similar behaviors and the same occurs for SL230a and TW. It is interesting to see that PRC45 follows the behavior of SLy230a and TW, although the binodal defined in terms of the pressure and proton fraction had a very different behavior. In the ρ_p versus ρ_n plane this

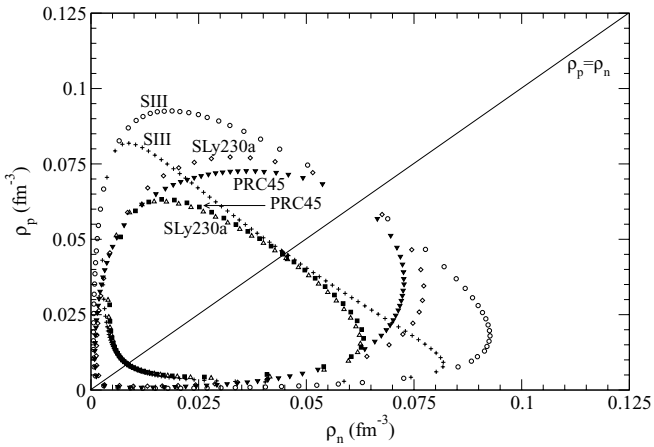

FIG. 5. Coexistence section (external curves) with spinodal section (internal curves) at $T = 10$ MeV.

difference is not so large but still reasonable, as can be seen in Fig. 5 where the spinodals and binodals are compared for the nonrelativistic models.

It is worth emphasizing some points mentioned in Ref. [32]. There are two possibilities of $\lambda_\pm$ eigenvalues. First, only one eigenvalue is negative, implying that a single order parameter is sufficient to describe the transition. Second, both eigenvalues are negative, implying that two independent order parameters should exist, indicating that more than two phases can coexist. For all models studied here, both relativistic and nonrelativistic, we have obtained only one negative eigenvalue, suggesting therefore the need for a single order parameter. In the context of asymmetric nuclear matter, it is a delicate question because it addresses the issue of the order of the phase transition itself either as first [32] or second order [33].

The region between the boundaries of the thermodynamical spinodal and the coexistence curve is defined as the metastability region. To illustrate this region, we present in Fig. 5 the thermodynamical spinodal and coexistence curve for each nonrelativistic model at some temperature, chosen to be $T = 10$ MeV. In this figure, the points where the spinodal and coexistence curves touch are symmetric with respect to the line $\rho_p = \rho_n$ and define a single value for ρ and y, which is precisely the critical point at the temperature for which the spinodal and binodal were obtained. These two points coalesce on a single point of the diagonal line at the maximum temperature for which there still is phase coexistence, which corresponds to the end point of the critical line. Let us remark that such symmetry is broken when one introduces the Coulomb interaction [22]. For relativistic models the same relation between the spinodals and binodals exists and the same considerations apply.

C. Charge-neutral matter

Proceeding with the comparison between relativistic and nonrelativistic models, we also investigate the thermodynamical instabilities of asymmetric charge-neutral matter. Here, electrons and neutrinos can be generated by β decay as well as by inverse β-decay processes. We assume that neutrinos escape this matter and, therefore, ($\mu_\nu = 0$) charge neutrality requires that $\mu_n = \mu_p + \mu_e$. At zero temperature μ_e is the relativistic Fermi energy of a Fermi gas, $\mu_e = \sqrt{k_{F_e}^2 + m_e^2}$. β equilibrium requires $k_{F_e} = k_{F_p}$ or, equivalently, $\rho_p = \rho_e$. Let us remark that a nonrelativistic limit of μ_e makes sense only when $k_{Fe} < m_e$, which leads to a region of negligible values for the density. Therefore, the electrons will be included only relativistically.

The pressure has to be calculated by including the electron kinetic term added to the nucleonic part, $\mathcal{E} = \mathcal{E}_N + \mathcal{E}_e$:

$$P = \rho \frac{\partial \mathcal{E}}{\partial \rho} - \mathcal{E}, \tag{31}$$

where $\mu_e = \frac{\partial \mathcal{E}_e}{\partial \rho}$.

From Fig. 4, without the β-equilibrium condition, one sees that the size of the thermodynamical instability region decreases as the temperature increases. Roughly speaking, the same should happen if one considers charge neutrality, since the addition of the electronic pressure to the nucleonic one would play the same role as an increase of the temperature in the nucleonic pressure alone. This behavior can be seen in Ref. [25] for different relativistic models. At $T = 0$, by imposing charge neutrality in the nonrelativistic models, the electron pressure is so strong that no thermodynamical instability was found. Consequently, within nonrelativistic models, the requirement of charge neutrality will also eliminate thermodynamical instability regions at finite temperature. At least for SLy230a, the failure to find a thermodynamical instability region in this context should come as no surprise, since the relativistic TW model, with which it shares a number of quantitative similarities [see Figs. 4(a) and 4(b)], does not present such a region either. For the other nonrelativistic models, which also turned out not to show this region, we had no prior expectations, because it is already known that thermodynamical instability with β equilibrium is strongly model-dependent [26] and shows up clearly in the other relativistic models studied here. Whether the absence of this instability region is a universal characteristic of all nonrelativistic models remains to be examined.

Although from the thermodynamical point of view, a static approach, neutral matter formed by neutrons, protons, and electrons would be stable, this is only a metastable configuration. Any perturbation would clusterize matter since such a configuration would have a smaller energy. For small clusters this would be a behavior similar to the one that occurs during a relativistic heavy-ion collision after a compound nucleus configuration. However, in stellar matter we may have new situations corresponding to the formation of large stable clusters.

D. Isospin distillation

In the study of asymmetric nuclear matter, there is an important observational scenario in which the gas phase becomes more neutron-rich than the liquid phase [34]. This happens for different nuclei with distinct proton/neutron ratios. Therefore, it is an important issue to investigate how this neutron-richness changes as a function of the nuclear density

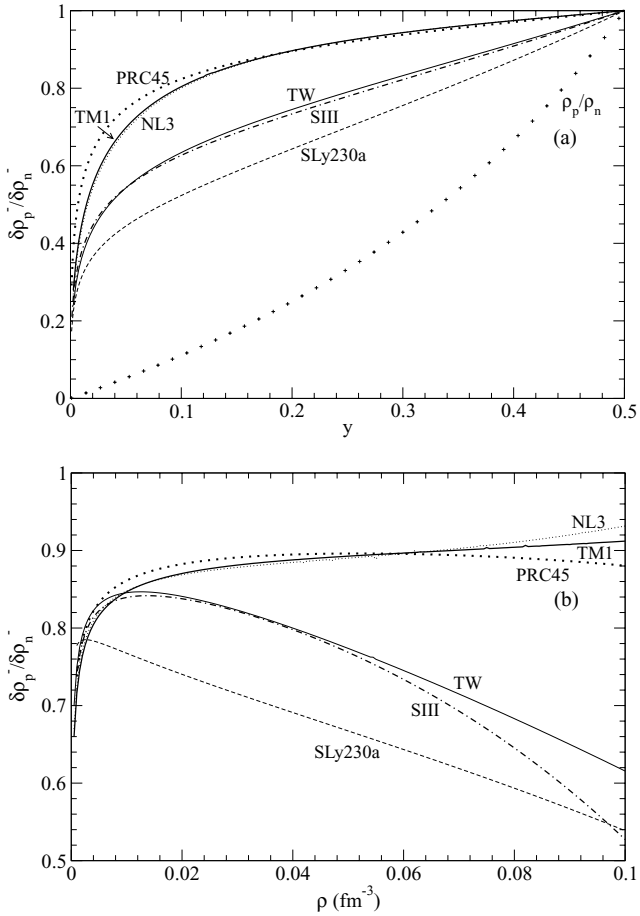

FIG. 6. The ratio $\delta\rho_p^-/\delta\rho_n^-$, at $T = 0$, as a function of (a) y with $\rho = 0.06$ fm^{-3} and (b) ρ with $y = 0.2$.

for a constant asymmetry parameter, as well as a function of the asymmetry itself for a constant value of the nuclear density. The quantity that allows this investigation is the ratio $\delta\rho_p/\delta\rho_n$. In principle, one could expect that this ratio would just follow the value of ρ_p/ρ_n that characterizes the matter under investigation. This is however not the case since, to minimize the energy, the system clusterizes in almost symmetric clusters immersed in a neutron-rich gas. The ratio $\delta\rho_p/\delta\rho_n$ gives exactly this information. By comparing this ratio for different models, we are able to discuss the fraction of protons of the large fragments and of the evaporated small fragments predicted by each one.

Next we plot the ratio $\delta\rho_p^-/\delta\rho_n^-$ given by Eq. (30) in Fig. 6 for all the models discussed in the present work. This is an important quantity since it measures the efficiency in restoring isospin symmetry: the larger its value, the greater the efficiency. In Fig. 6(a), the ratio $\delta\rho_p^-/\delta\rho_n^-$ is plotted as a function of the proton fraction with $\rho = 0.06$ fm^{-3} and in Fig. 6(b) it is plotted as a function of the density with $y = 0.2$ at $T = 0$ MeV in both cases.

One can see from Fig. 6(a) that the TW parametrization of the DDHM has the smaller ratios of $\delta\rho_p^-/\delta\rho_n^-$ among the relativistic models. Although still larger than ρ_p/ρ_n, the restoration of isospin symmetry in liquid nuclear matter is not as efficient as in NL3 and TM1, except for the very low densities. At subsaturation densities the symmetry energy of the TW model is larger than the one of the NL3 model, as seen from Fig. 1. This explains the behavior of the distillation effect at very low densities, which is larger for TW than for NL3. Moreover, although for NL3 and TM1 the ratio $\delta\rho_p^-/\delta\rho_n^-$ increases with ρ and attains values larger than 0.85 for $\rho > 0.03$ fm^{-3}, the opposite occurs for TW: The ratio $\delta\rho_p^-/\delta\rho_n^-$ in the latter decreases with density, reaching values below 0.7 at the larger density values in the unstable region. This behavior is in accordance with the results obtained in Ref. [32] within the density functional formalism with Skyrme and Gogny effective forces.

Regarding the nonrelativistic models, the situation is as follows. Now, instead of SLy230a, it is SIII that better approaches the relativistic TW model. However, the similarity occurs only for densities smaller than 0.05 fm^{-3} since the slope is different. The ratio $\delta\rho_p^-/\delta\rho_n^-$ is smaller for SLy230a, but it presents the same kind of slope as TW. Looking back at Fig. 1 for densities below 0.1 fm^{-3}, we see that the symmetry energy has similar values for all the models, but the slope is quite different. A comparison of the first and second derivatives of the symmetry energy is important to understand the similarities and differences among the models. Note also how NL3, TM1, and PRC45 become similar.

The fact that similar behavior for the symmetry energy, critical points, spinodal, and coexistence curves followed by SLy230a and TW breaks down when we consider the efficiency to restore isospin symmetry seems to be new and interesting. Again, it shows that all the models have to be investigated in as many as possible properties before one could predict results. Our numbers robustly suggest that the isospin distillation effect is strongly uncorrelated with other known bulk properties and has to be taken into consideration when selecting nuclear models for asymmetric nuclear matter. This finding has surprised us, since it is known that fractionation should reflect the features of the symmetry energy in nuclear matter [35]. Notice here that, even for quantities such as L and $K_{\rm sym}$, which are expected to better reflect the features of the very low density regime, it is still SLy230a, the nonrelativistic model, that more closely approaches TW as seen in Table II.

E. Stellar matter nucleation

In Fig. 7 we show the EoS for stellar matter in β equilibrium for the relativistic NL3 and TW models [Figs. 7(a) and 7(b)] and the nonrelativistic SLy230a model [Fig. 7(c)]. Whenever it crosses the spinodal curve, a region of nucleation is expected to show up at the crust of the star. One can see that, for NL3 at $T = 0$, this is the case. However, at $T = 10$ MeV, the EoS for stellar matter does not cross the corresponding spinodal. The same behavior is seen for TM1 (not shown) and TW, for which the crossing occurs at a larger density at $T = 0$ than for NL3. At finite temperatures, one could expect that the stellar EoS could include trapped neutrinos. Indeed, if these are considered, the related EoS also crosses the respective spinodal, as can be seen in Ref. [36], and the nonhomogeneous phase is then also expected. In Fig. 7(c), we see that the SLy230a model, following the relativistic ones, also crosses

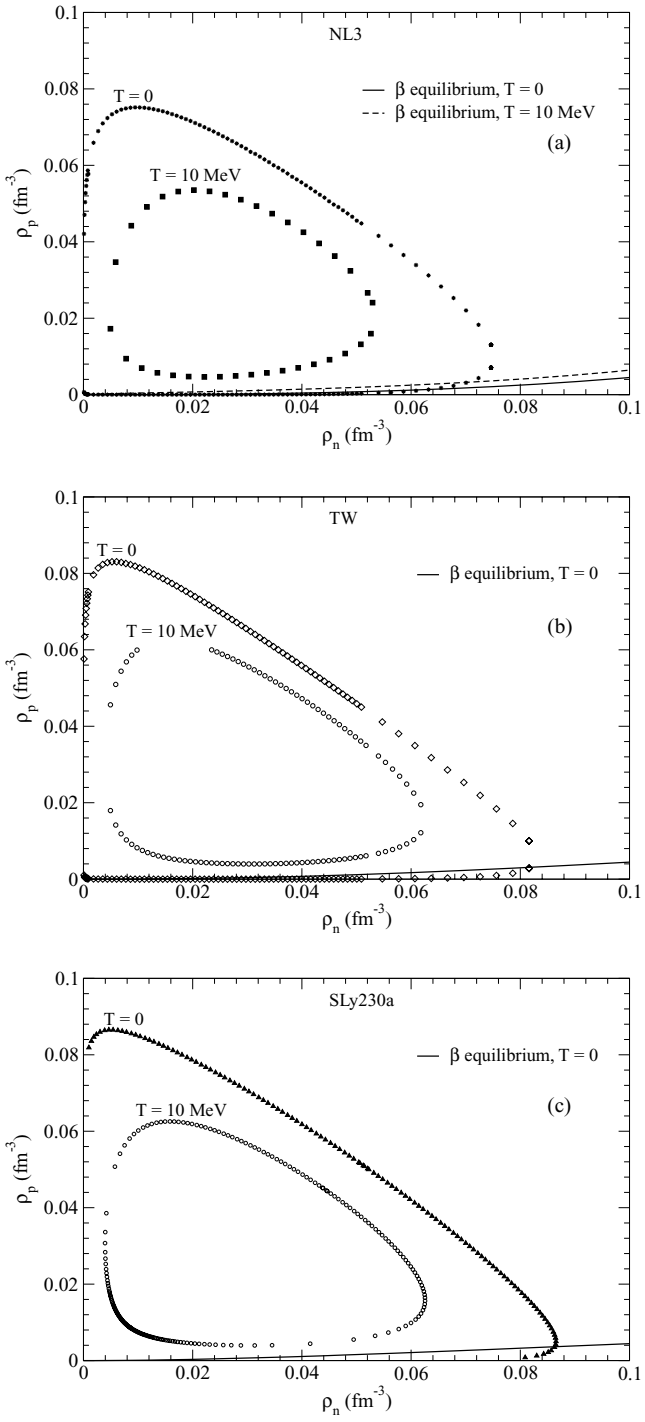

FIG. 7. Spinodal section at $T = 0$ and the β-equilibrium EoS solution, $\mu_n = \mu_p + \mu_e$ for (a) NL3, (b) TW, and (c) SLy230a.

the spinodal curve at $T = 0$. In this aspect, let us remark that PRC45, as well as SIII, also presents the same feature (not shown). Therefore, relativistic and nonrelativistic models have indicated the possibility of describing the instability region in stellar matter at zero temperature. In this section, we have only considered thermodynamical instabilities. The densities at the inner edge of the crust of a neutron star should be determined by including the electron contribution and dynamical instabilities. It has, however, been shown that the instability region is only slightly smaller, so the values obtained already give a good preview of an upper limit.

TABLE IV. Densities and proton fraction for the crossing between stellar matter EoS and spinodal.

	ρ_p (fm^{-3})	ρ_n (fm^{-3})	ρ (fm^{-3})	y
SIII	0.0051	0.111	0.1161	0.044
SLy230a	0.0033	0.086	0.0893	0.037
PRC45	0.0058	0.081	0.0868	0.067
NL3	0.0014	0.064	0.0654	0.021
TM1	0.0017	0.068	0.0697	0.024
TW	0.0032	0.082	0.0852	0.037

Here, let us mention that, since the regions bounded by the spinodal at $T = 0$ are larger than those for finite temperature, the figures show the upper density limits for the instability we are discussing. By studying the inner boundary of a neutron-star crust [37], the transition between matter in the crust of a neutron star and the uniform matter in its interior was found to be at $\rho \approx 0.09$ fm^{-3}. If we use $\rho = \rho_n + \rho_p$ where the stellar matter EoS crosses the spinodal in Fig. 7, we get results close to that, particularly for the TW, SLy230a, and PRC45 models (see Table IV). The TW and SLy230a models also show the same proton fraction.

V. EOS HIGH-DENSITY BEHAVIOR

Up to now we have restricted our study of models for asymmetric nuclear matter to the regime of small temperature and small nuclear densities. Studies of relativistic hadronic models at the extreme regime of density and temperature have been largely studied in connection to quark-gluon plasma phase transition [38]. It is natural that, the more the density and the temperature increase, the more the hadronic models differ, since they were built to fit nuclear matter observables measured at the saturation density ρ_0 and zero temperature. To compress nuclear matter in the laboratory is a difficult task and can only be achieved through very high energy heavy-ion collision experiments [19,39]. In the very beginning of the reaction, before expansion and freeze-out, projectile and target overlap in a very small phase space volume, or, equivalently, in a very high dense matter regime. For a very short time, a sample of what may happen in neutron stars and core-collapse supernovae is created.

In a very important recent work [19], measured values for the directed transverse flow in collisions of ^{197}Au nuclei at incident kinetic energy per nucleon varying from about 0.15 to 10 GeV were analyzed. This study allowed the authors to extrapolate the available data [40] for pressure at about $2\rho_0$ to higher values of density for symmetric infinite nuclear matter, as well as for neutron matter. Notice that the ^{197}Au isotope has approximately the same asymmetry parameter y as that of supernovae, being distinct from that of neutron matter ($y = 0$) and symmetric nuclear matter ($y = 1/2$). The extrapolation for such matter has taken into account the uncertainty bands of the

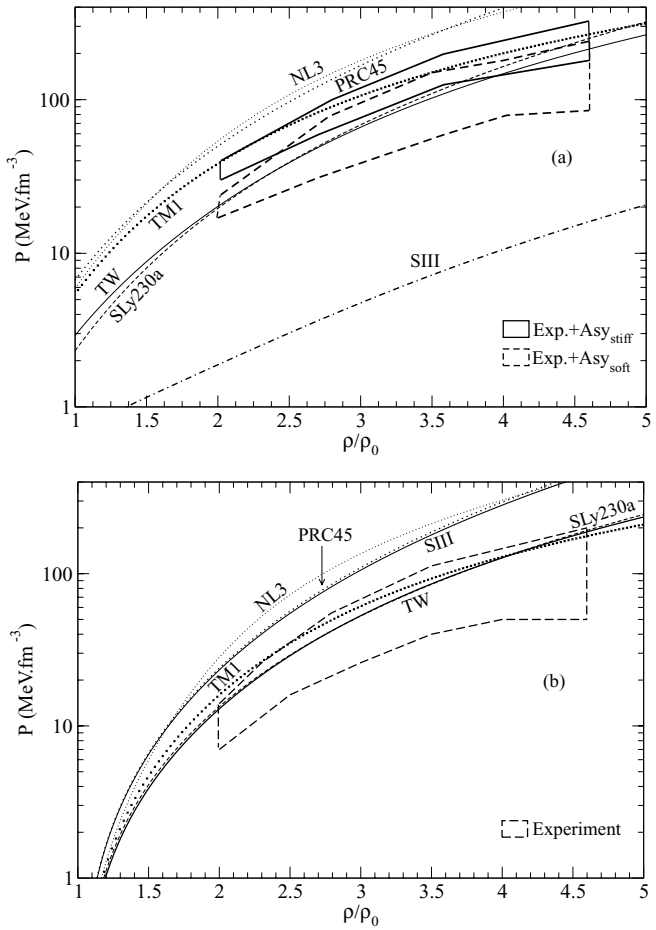

FIG. 8. Pressure, in log scale, versus ρ/ρ_0 at $T = 0$ for the relativistic and nonrelativistic models: (a) curves for neutron matter; (b) curves for symmetric matter. The band regions were extracted from Ref. [19].

weakest (Asy_{soft}) and strongest (Asy_{stiff}) density dependence of the symmetry energy proposed [41], since experimental data for symmetry energy at $\rho > \rho_0$ are still poor [19].

In Fig. 8 we present the proposed experimental constraints for neutron matter and symmetric nuclear matter, respectively [19], together with results from the models we have studied.

In face of this result, only a few nuclear models fit the two extreme experimental soft-stiff bands assigned as acceptable for neutron matter theoretical model calculations. As we can see, TW, TM1, and Sly230a data lie inside these bands. In the case of symmetric nuclear matter, again the same models fulfill this experimental constraint. At high density TM1 behaves differently from NL3 owing to its nonlinear ω-meson term.

VI. CONCLUSIONS

We have studied nuclear nonrelativistic and relativistic models for asymmetric nuclear matter. These models have been compared for different applications. From the zero-temperature regime, in which their free parameters are adjusted from nuclear matter bulk properties, up to the finite-temperature regime, we studied the stable coexistence regime, critical parameters, metastable spinodal regions, neutron-matter in β equilibrium, and isospin distillation. At $T = 0$ MeV, the high-density regime predicted from the models was confronted with experimental predictions [19]. We can summarize our main findings as follows:

(i) The models studied differ in relation to their symmetry energy as the density increases. Figure 1 signals that this difference becomes extreme when we compare the nonrelativistic SIII and PRC45 models, for which the symmetry energy has opposing slopes at high densities.

(ii) The phase coexistence regions displayed in Fig. 3 also differ. These differences are also present on the symmetric nuclear matter critical temperature shown in Table III. The binodal surface of SLy230a approaches that of the relativistic models, whereas that of the other nonrelativistic models do not.

(iii) The spinodal curves plotted in Fig. 4 delimit the instability region. Such curves can be put inside the coexistence region, the binodals, as seen in Fig. 5. The region between both defines the metastability region predicted by each model. For each different model, stability, instability and metastability regions move together. These regions for the nonrelativistic SLy230a approach well those obtained with the relativistic TW model.

(iv) By studying the charge-neutral matter with the β-equilibrium process, no instability region was found for the nonrelativistic models. In other words, no spinodal region, even at $T = 0$ MeV, was obtained. It is, however, not the case for the relativistic models we studied since, among them, only the TW model lies in the same situation as the nonrelativistic ones.

(v) The study of isospin distillation has surprised us. The relativistic TW and the nonrelativistic SLy230a, which gave similar behaviors for other nuclear properties as well as in the spinodals and in the coexistence phase regime, as seen in Figs. 1, 3, and 4, became not so close when we considered restoration of the isospin symmetry, although they did show the same slope, as seen in Fig. 6. In contrast, SIII, which, for the other nuclear properties, was quite different from the TW model, has approached it in this kind of instability. The same occurred for the PRC45, TM1, and NL3 models. Therefore, we consider that this instability is strongly model dependent and this issue shall be addressed in further investigations.

(vi) We used all the models in a simplified stellar matter modeling and have investigated whether β-equilibrium EoS crosses the spinodal as shown in Fig. 7. Whenever it does, a region of nucleation is expected at the crust of the star. We have seen that at $T = 0$ MeV, SLy230a, TW, and PRC45 EoSs (see Table IV) cross the spinodal curve at about $\rho_n = 0.08$ fm^{-3} and $\rho = \rho_n + \rho_p \approx 0.09$ fm^{-3}, close to the results obtained for some interactions of Ref. [37]. At $T = 10$ MeV, none of the models show the crossing, and the nonhomogeneous matter is not expected to exist in warm stellar matter without trapped neutrinos. Had neutrino trapping been

included, the situation would be different: The proton fraction would be close to 0.3 and the EoS would cross the spinodal region [42]. Therefore, relativistic and nonrelativistic models have indicated the possibility of describing the instability region in stellar matter for zero temperature. Here, we ask the same question as posed in Ref. [37]: How is the transition density related to other nuclear properties?

(vii) For the high-density regime (see Fig. 8), the models that simultaneously fit the experimental predictions better for neutron matter and symmetric nuclear matter [19] are TW, TM1, and SLy230a.

The study we have performed helps in our understanding of relativistic and nonrelativistic equations of state, their similarities, discrepancies, and model dependencies. There is no specific particularity in our results that favors the relativistic description of asymmetric nuclear matter, other than having a sound theoretical basis and completeness. By handling different parametrizations to fit different data, they reveal discrepancies as we investigate more physical quantities. More data are needed in to develop better selection criteria among all these models. A full understanding of how one EoS deviates from another with similar values for the bulk properties (such as, for example, SLy230a and TW) is still lacking.

ACKNOWLEDGMENTS

This work was partially supported by CNPq (Brazil) and CAPES (Brazil) and by FEDER/FCT (Portugal) under the projects POCI/FP/63918/2005 and PTDC/FIS/64707/2006.

APPENDIX

Here we give the steps to prove that both criteria for the determination of the instability boundary, given by Eqs. (26) and (28), are equivalent. Assuming that g is an arbitrary function and using the Jacobi determinant for the transformation from the variables (ρ, y) to the variables (ρ_p, ρ_n), one obtains

$$\left.\frac{\partial g}{\partial \rho}\right|_y = \frac{\partial(g,y)}{\partial(\rho,y)} = \frac{\partial(g,y)}{\partial(\rho_p,\rho_n)}\frac{\partial(\rho_p,\rho_n)}{\partial(\rho,y)} = \frac{1}{\rho}\left[\rho_p \left.\frac{\partial g}{\partial \rho_p}\right|_{\rho_n} + \rho_n \left.\frac{\partial g}{\partial \rho_n}\right|_{\rho_p}\right] \tag{A1}$$

and

$$\left.\frac{\partial g}{\partial y}\right|_\rho = \rho\left[\left.\frac{\partial g}{\partial \rho_p}\right|_{\rho_n} - \left.\frac{\partial g}{\partial \rho_n}\right|_{\rho_p}\right]. \tag{A2}$$

By substituting $P = -f + \mu_p\rho_p + \mu_n\rho_n$ into Eq. (26) and using Eqs. (A1) and (A2) it follows that

$$\begin{aligned} 0 &= \left.\frac{\partial P}{\partial \rho}\right|_{T,y}\left.\frac{\partial \mu_q}{\partial y}\right|_{T,\rho} - \left.\frac{\partial \mu_q}{\partial \rho}\right|_{T,y}\left.\frac{\partial P}{\partial y}\right|_{T,\rho} \\ &= \rho\left[\left(\left.\frac{\partial \mu_p}{\partial \rho_n}\right|_{\rho_p}\rho_p + \left.\frac{\partial \mu_n}{\partial \rho_n}\right|_{\rho_p}\rho_n\right)\left.\frac{\partial \mu_q}{\partial \rho_p}\right|_{\rho_n} \right. \\ &\quad \left. - \left(\left.\frac{\partial \mu_p}{\partial \rho_p}\right|_{\rho_n}\rho_p + \left.\frac{\partial \mu_n}{\partial \rho_p}\right|_{\rho_n}\rho_n\right)\left.\frac{\partial \mu_q}{\partial \rho_n}\right|_{\rho_p}\right], \quad q = p, n. \end{aligned}$$

Taking $q = n$ (or, equivalently, $q = p$) in this equation, we recover the criterion given in Eq. (28) for the instability boundaries.

[1] P. Ring and P. Schuck, *The Nuclear Many-Body Problem* (Springer, Heidelberg, 1980); R. Machleidt, Adv. Nucl. Phys. **19**, 189 (1989); A. Akmal and V. R. Pandharipande, Phys. Rev. C **56**, 2261 (1997).

[2] F. Coester, S. Cohen, B. D. Day, and C. M. Vincent, Phys. Rev. C **1**, 769 (1970); A. Delfino, J. B. Silva, and M. Malheiro, *ibid.* **73**, 037311 (2006).

[3] S. Typel and H. H. Wolter, Nucl. Phys. **A656**, 331 (1999); H. Lenske and C. Fuchs, Phys. Lett. **B345**, 355 (1995); C. Fuchs, H. Lenske, and H. H. Wolter, Phys. Rev. C **52**, 3043 (1995).

[4] D. Vautherin and D. M. Brink, Phys. Rev. C **5**, 629 (1972).

[5] B. D. Serot and J. D. Walecka, Adv. Nucl. Phys. **16**, 1 (1986).

[6] S. K. Adhikari, T. Frederico, and I. D. Goldman, Phys. Rev. Lett. **74**, 487 (1995).

[7] A. Delfino, T. Frederico, V. S. Timóteo, and L. Tomio, Phys. Lett. **B634**, 185 (2006).

[8] L. H. Thomas, Phys. Rev. **47**, 903 (1935); V. Efimov, Phys. Lett. **B33**, 563 (1970).

[9] T. H. R. Skyrme, Philos. Mag. **1**, 1043 (1956); Nucl. Phys. **9**, 615 (1959).

[10] G. Gelmini and B. Ritzi, Phys. Lett. **B33**, 563 (1970); A. Delfino, M. Malheiro, and T. Frederico, Braz. J. Phys. **31**, 518 (2001).

[11] G. A. Lalazissis, J. König, and P. Ring, Phys. Rev. C **55**, 540 (1997).

[12] K. Sumiyoshi, H. Kuwabara, and H. Toki, Nucl. Phys. **A581**, 725 (1995).

[13] T. Gaitanos, M. Di Toro, S. Typel, V. Baran, C. Fuchs, V. Greco, and H. H. Wolter, Nucl. Phys. **A732**, 24 (2004).

[14] T. Niksic, D. Vretenar, P. Finelli, and P. Ring, Phys. Rev. C **66**, 024306 (2002); D. Vretenar, T. Niksic, and P. Ring, *ibid.* **68**, 024310 (2003).

[15] C. J. Horowitz and J. Piekarewicz, Phys. Rev. C **64**, 062802(R) (2001); J. K. Bunta and S. Gmuca, *ibid.* **68**, 054318 (2003); **70**, 054309 (2004).

[16] J. Boguta and S. I. Moszkowski, Nucl. Phys. **A403**, 445 (1983).

[17] R. J. Furnstahl, J. J. Rusnak, and B. D. Serot, Nucl. Phys. **A632**, 607 (1998).

[18] C. Providência, D. P. Menezes, L. Brito, and Ph. Chomaz, nucl-th/0704.3607.

[19] P. Danielewicz, R. Lacey, and W. G. Lynch, Science **298**, 1592 (2002).

[20] E. Chabanat, P. Bonche, P. Haensel, J. Meyer, and R. Schaeffer, Nucl. Phys. **A627**, 710 (1997).

[21] K. Huang, *Statistical Mechanics* (Wiley, New York, 1963).

[22] S. J. Lee and A. Z. Mekjian, Phys. Rev. C **63**, 044605 (2001); **45**, 1284 (1992).

[23] W. D. Myers and W. J. Swiatechi, Ann. Phys. (NY) **55**, 395 (1969); K. C. Chung, C. S. Wang, A. J. Santiago, and J. W. Zhang, Phys. Rev. C **61**, 047303 (2000).

[24] W. D. Myers and W. J. Swiatechi, Nucl. Phys. **A601**, 141 (1996); K. C. Chung, C. S. Wang, and A. J. Santiago, Europhys. Lett. **47**, 663 (1999).

[25] S. S. Avancini, L. Brito, D. P. Menezes, and C. Providência, Phys. Rev. C **70**, 015203 (2004).
[26] S. S. Avancini, L. Brito, Ph. Chomaz, D. P. Menezes, and C. Providencia, Phys. Rev. C **74**, 024317 (2006).
[27] S. S. Avancini, J. R. Marinelli, D. P. Menezes, M. M. W. Moraes, and C. Providência, Phys. Rev. C **75**, 055805 (2007).
[28] J. Margueron, J. Navarro, and N. V. Giai, Phys. Rev. C **66**, 014303 (2002).
[29] M. Barranco and J. R. Buchler, Phys. Rev. C **22**, 1729 (1980); J. M. Lattimer and D. G. Ravenhall, Astrophys. J. **223**, 314 (1978).
[30] D. P. Menezes and C. Providência, Nucl. Phys. **A650**, 283 (1999); G. Krein, D. P. Menezes, M. Nielsen, and C. Providência, *ibid.* **A674**, 125 (2000) .
[31] D. P. Menezes and C. Providência, Phys. Rev. C **60**, 024313 (1999).
[32] J. Margueron and P. Chomaz, Phys. Rev. C **67**, 041602(R) (2003).
[33] H. Muller and B. D. Serot, Phys. Rev. C **52**, 2072 (1995).
[34] H. S. Xu *et al*., Phys. Rev. Lett. **B85**, 716 (2000).
[35] A. Ono, P. Danielewicz, W. A. Friedman, W. G. Lynch, and M. B. Tsang, Phys. Rev. C **68**, 051601(R) (2003).
[36] C. Providência, L. Brito, A. M. S. Santos, D. P. Menezes, and S. S. Avancini, Phys. Rev. C **74**, 045802 (2006); L. Brito, C. Providência, A. M. Santos, S. S. Avancini, D. P. Menezes, and Ph. Chomaz, *ibid.* **74**, 045801 (2006); C. Providência, L. Brito, S. S. Avancini, D. P. Menezes, and Ph. Chomaz, *ibid*. **73**, 025805 (2006); S. S. Avancini, L. Brito, D. P. Menezes, and C. Providência, *ibid*. **71**, 044323 (2005).
[37] C. J. Pethick, D. G. Ravenhall, and C. P. Lorenz, Nucl. Phys. **A584**, 675 (1995).
[38] H. Stocker and W. Greiner, Phys. Rep. **137**, 277 (1986); R. J. Furnstahl, B. D. Serot, and T. Hua-Bin, Nucl. Phys. **A615**, 441 (1997); A. Delfino, M. Chiapparini, M. E. Bracco, L. Castro, and S. E. Epsztein, J. Phys. G: Nucl. Part. Phys. **27**, 2251 (2001); A. Delfino, J. B. Silva, M. Malheiro, M. Chiapparini, and M. E. Bracco, *ibid*. **28**, 2249 (2002).
[39] H. Satz, Rep. Prog. Phys. **63**, 1511 (2000); P. Braun-Munzinger, D. Magestro, R. Redlich, and J. Stachel, Phys. Lett. **B518**, 41 (2001).
[40] D. Brill *et al*., Z. Phys. A **355**, 61 (1996).
[41] M. Prakash, T. L. Ainsworth, and J. M. Lattimer, Phys. Rev. Lett. **61**, 2518 (1988).
[42] L. Brito, C. Providência, A. M. Santos, S. S. Avancini, D. P. Menezes, and Ph. Chomaz, Phys. Rev. C **74**, 045801 (2006).